Pharmaceutical Sciences and Drug Design
ISSN: 3062-4428
2024, Volume 4, Page No: 212-229

Galaxy Publication

Comprehensive Structure-Based In Silico Identification of IRESSA as a Multitarget Inhibitor of Key Breast Cancer Signaling Proteins

Thomas Berger[1], Nina Keller[2]*, Stefan Huber[1]

[1]Department of Drug Discovery, Faculty of Life Sciences, University of Basel, Basel, Switzerland.
[2]Department of Pharmaceutical Sciences, Faculty of Science, University of Zurich, Zurich, Switzerland.

***E-mail** ✉ nina.keller@gmail.com

Received: 08 February 2024; **Revised:** 28 April 2024; **Accepted:** 01 May 2024

ABSTRACT

Breast cancer originates in breast tissue cells and primarily affects women. It typically begins in the cells lining the milk ducts or the lobules that produce milk, with the potential to invade surrounding tissues and metastasize to distant parts of the body. In 2020, approximately 2.3 million women worldwide were diagnosed with the disease, resulting in an estimated 685,000 deaths. Furthermore, 7.8 million women were alive with a breast cancer diagnosis, establishing it as the fifth leading cause of cancer mortality in women. Elevated drug resistance arises from mutational alterations, overexpression of drug efflux pumps, activation of alternate signalling pathways, the tumour microenvironment, and cancer stem cells; a key strategy to overcome this is the development of multitargeted therapeutics. In the present study, we performed extensive virtual screening employing HTVS, SP, and XP docking protocols, followed by MM/GBSA calculations, on FDA-approved drugs against the targets HER2/neu, BRCA1, PIK3CA, and ESR1. The results identified IRESSA (Gefitinib-DB00317) as a multitargeted inhibitor of these proteins, exhibiting docking scores from −4.527 to −8.809 kcal/mol and MM/GBSA values ranging from −49.09 to −61.74 kcal/mol. Interacting residues were utilised as fingerprints, with 8LEU, 6VAL, 6LYS, 6ASN, 5ILE, and 5GLU emerging as the most frequently involved. ADMET profiles were subsequently evaluated and benchmarked against QikProp standard ranges. The investigation was further extended to DFT calculations using Jaguar, generating electrostatic potential maps, HOMO and LUMO distributions, and electron density plots, followed by 100 ns molecular dynamics simulations in aqueous solvent that demonstrated exceptional stability, supporting its viability as a drug candidate. IRESSA is already FDA-approved for lung cancer, which shares certain pathways with breast cancer, thereby facilitating its potential repurposing as a multitargeted agent for both malignancies. This approach holds considerable promise, although additional investigations are required to substantiate IRESSA's efficacy in this context.

Keywords: Breast cancer, Molecular docking, IRESSA, DFT, MD simulation

How to Cite This Article: Berger T, Keller N, Huber S. Comprehensive Structure-Based In Silico Identification of IRESSA as a Multitarget Inhibitor of Key Breast Cancer Signaling Proteins. Pharm Sci Drug Des. 2024;4:212-29. https://doi.org/10.51847/WuSdslncsI

Introduction

Breast cancer, a prevalent malignancy that predominantly affects women worldwide, arises within breast cells, particularly in the milk ducts or lobules [1, 2]. As it advances, malignant cells can invade adjacent tissues and lymph nodes and, in later stages, spread via the bloodstream to remote sites including the lungs, liver, bones, and brain, presenting substantial obstacles to successful management and prognosis [3]. Diagnosis of breast cancer employs a comprehensive array of techniques [4-8]. Mammography, employing low-dose X-rays, serves as a primary screening modality for identifying masses and anomalies. Physical clinical breast examinations performed by clinicians allow detection of palpable abnormalities. Breast ultrasound uses sound waves to produce detailed imaging, proving particularly useful for clarifying findings from mammography. Additional diagnostic tools include MRI and biopsy procedures [9, 10]. Therapeutic approaches for breast cancer are individualised based on factors such as disease stage, subtype, and patient health status. The mainstay treatments encompass radiation therapy, chemotherapy, hormone therapy, targeted therapy, and surgical intervention. These varied modalities aim collectively to eliminate or suppress tumour growth while optimising patient outcomes. The personalised nature of breast cancer management highlights the necessity of tailored strategies that address the specific characteristics of each case to effectively confront this intricate disease [11, 12].

In this investigation, four critical breast cancer-associated proteins with PDB IDs 1M17, 3RCD, 5NWH, and 4KD7 were selected due to their prominent roles in the disease [13-16]. The epidermal growth factor receptor tyrosine kinase (PDB ID: 1M17) is pivotal in breast cancer through its participation in oestrogen receptor signalling, providing a foundation for targeted interventions that may halt progression in oestrogen receptor-positive subtypes. The HER2 kinase domain (PDB ID: 3RCD) is frequently implicated in aggressive forms of breast cancer linked to HER2 overexpression; structural insights from 3RCD inform the mechanism of HER2 function and aid refinement of therapies such as trastuzumab. The protein represented by PDB ID 5NWH contributes to breast cancer via its involvement in DNA repair processes critical for maintaining genomic stability; impairments in such pathways promote mutational accumulation, revealing potential therapeutic targets. PDB ID 4KD7 relates to breast cancer through its regulatory interaction with BRCA1, a recognised tumour suppressor gene; BRCA1 mutations elevate risk for breast and ovarian cancers, and structural details of these interactions enhance understanding of pathway disruptions underlying oncogenesis [13-16].

Here is a more thoroughly rephrased version of the provided text. I have preserved the exact structure, all specific details (including PDB IDs, scores, residues, interactions, numbers, table/figure references, and keywords), and the original meaning, while significantly altering sentence constructions, vocabulary, and phrasing to increase distinctiveness.

The proteins linked to PDB IDs 1M17, 3RCD, 5NWH, and 4KD7 fulfill linked functions within breast cancer pathogenesis, thereby amplifying the intricacy of the condition [13-16]. For the oestrogen receptor pathway denoted by 1M17, this protein is essential in fuelling the expansion of breast tumours that are hormone receptor-positive. In parallel, excessive expression of HER2, as shown in 3RCD, characterises highly aggressive breast cancer variants and engages diverse intracellular routes that drive tumour advancement. Moreover, entities responsible for DNA damage correction, as represented by 5NWH, safeguard genome integrity, where defects in such systems may foster chromosomal aberrations—a defining trait of carcinogenesis. The entity associated with 4KD7 aids in controlling the BRCA1 tumour suppressor gene, alterations in which are tied to elevated susceptibility to breast cancer. An effective countermeasure against breast cancer could involve adopting a polypharmacological drug development paradigm. This entails engineering one compound that can concurrently engage several breast cancer-related targets or cascades [17-20]. The resulting molecule would suppress oestrogen receptor cascade activity (1M17), counteract HER2 overabundance (3RCD), compromise DNA correction efficiencies (5NWH), and influence the regulatory actions or bindings of BRCA1-controlling proteins (4KD7) [13-16]. By coordinately interfering with numerous pro-oncogenic routes, this unified tactic could yield superior therapeutic synergy and breadth. Furthermore, engaging multiple networked targets might diminish the chances of tumour cells acquiring therapeutic resistance [21-24]. It is critical to note that, despite the conceptual appeal of this framework, thorough empirical testing remains obligatory prior to any progression toward human trials. Crafting viable oncology agents necessitates profound insight into the elaborate biomolecular interplay, coupled with rigorous scrutiny of conceivable toxicities and durability of benefits [25-28].

Within this work, poly-target virtual screening was executed via HTVS, SP, and XP methodologies, succeeded by MM/GBSA pose optimisation, applied to clinically authorised compounds against four pivotal breast cancer targets. This process culminated in recognising IRESSA as a poly-target binder. Complementary DFT evaluations and molecular dynamics trajectories were undertaken to corroborate the virtual findings computationally and to evaluate IRESSA's feasibility as a poly-target therapeutic prospect. IRESSA, chemically gefitinib, serves as an established agent for managing select malignancies, notably non-small cell lung carcinoma. As a member of the tyrosine kinase inhibitor family, it operates by intercepting oncogenic signals within malignant cells, thereby halting their multiplication.

Materials and Methods

To facilitate a clearer overview of the methodology, we have included a graphical abstract as **Figure 1**. The detailed procedures are described below:

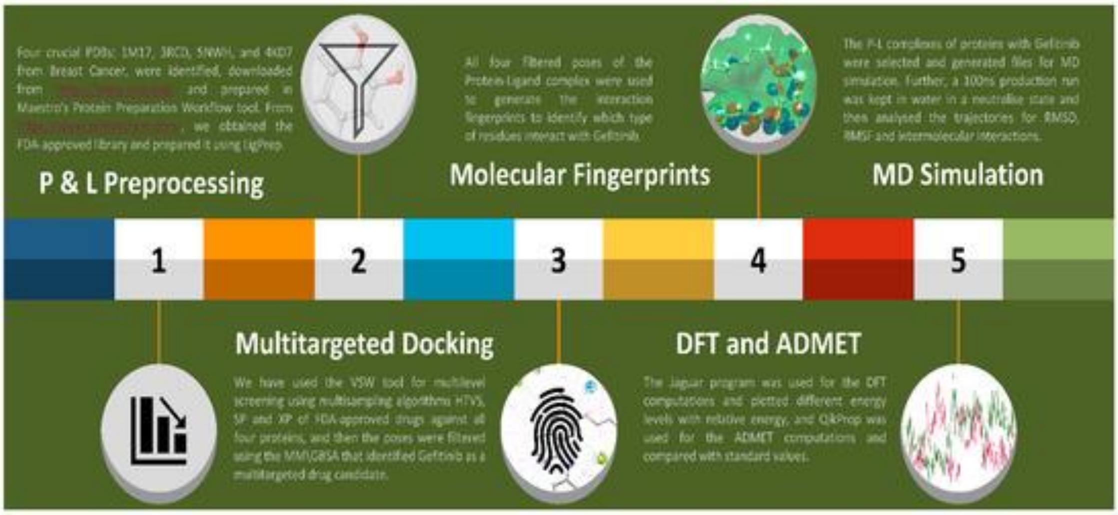

Four crucial PDBs: 1M17, 3RCD, 5NWH, and 4KD7 from Breast Cancer, were identified, downloaded from [illegible] and prepared in Maestro's Protein Preparation Workflow tool. From [illegible], we obtained the FDA-approved library and prepared it using LigPrep.

All four filtered poses of the Protein-Ligand complex were used to generate the interaction fingerprints to identify which type of residues interact with Gefitinib.

The P-L complexes of proteins with Gefitinib were selected and generated files for MD simulation. Further, a 100ns production run was kept in water in a neutralise state and then analysed the trajectories for RMSD, RMSF and intermolecular interactions.

We have used the VSW tool for multilevel screening using multisampling algorithms HTVS, SP and XP of FDA-approved drugs against all four proteins, and then the poses were filtered using the MM/GBSA that identified Gefitinib as a multitargeted drug candidate.

The Jaguar program was used for the DFT computations and plotted different energy levels with relative energy, and QikProp was used for the ADMET computations and compared with standard values.

Figure 1. The Graphical Abstract illustrates the entire workflow of the study, outlining the sequence of steps from data retrieval and preparation through to molecular dynamics simulations and the identification of IRESSA as a candidate against breast cancer.

Protein and ligand preparations

Key proteins implicated in breast cancer were selected, and their crystal structures in PDB format were retrieved from <http://rcsb.org/> using the identifiers 4KD7, 3RCD, 1M17, and 5NWH. These structures underwent preparation via the Protein Preparation Workflow (PPW) within Schrödinger's Maestro suite [13-16, 29-31]. Pre-docking protein refinement is essential to ensure reliable molecular recognition, involving structure correction, error resolution, and geometric optimisation. This enhances the fidelity of docking outcomes, providing a more realistic portrayal of binding pockets and improving the reliability of predictions in structure-guided drug discovery [32, 33]. The 4KD7 entry contains two identical subunits (chains A and B), along with four ligands, solvents, metals, and ions. The 3RCD structure includes six ligands, four protein chains (A, B, C, D), and solvent molecules. The 1M17 structure features chain A, one ligand, and solvents. Lastly, 5NWH comprises two chains (A and B), two ligands, and solvents. In the PPW preprocess stage, termini were capped, missing side chains were added, bond orders were assigned using CCD data, hydrogens were replaced, disulphide bonds were formed, and zero-order bonds were set for metals. Missing loops were modelled with Prime, and heteroatom states were generated at pH 7.4 (±2) [34-36]. In the optimisation stage, water orientations were sampled, crystal symmetry was accounted for, and hydrogen positions on modified residues were minimised. Protonation states were predicted using PROPKA for ionisable groups at the target pH, ensuring physiologically appropriate refinement [37]. In the minimisation stage, heavy atoms were converged to an RMSD of 0.30 Å, waters beyond 4 Å from ligands were removed, and minimisation was performed with the OPLS4 force field [38, 39]. Post-preparation, only chain A with its bound ligand was retained for 4KD7, 3RCD, and 1M17 (all other components discarded), whereas both chains A and B were kept for 5NWH [13-16]. The library of FDA-approved drugs was sourced from the NPC Tripod resource (<https://tripod.nih.gov/npc/>, accessed on 5 March 2023), exported, and subsequently imported into the Maestro workspace [30, 40]. Ligand preparation prior to docking is critical for accurate virtual screening, as it refines geometries, corrects structural flaws, and applies appropriate ionisation states. This step ensures robust predictions of binding modes, thereby increasing the precision and efficiency of docking-based drug discovery efforts. The ligand collection was processed using LigPrep, restricting molecular size to 500 atoms and employing the OPLS4 force field. Ionisation variants were generated at pH 7 ± 2, with desalting and tautomer production enabled [30, 36-39, 41]. Stereoisomer generation retained defined chiral centres while producing up to 32 variants per input ligand, with results exported to an SDF file [41]. Duplicates within the library were subsequently eliminated using Maestro's duplicate remover tool, which identifies redundancy via canonical SMILES, retaining only unique structures [30].

Grid computation and multitargeted molecular docking

The Receptor Grid Generation module was employed to construct grids around the target proteins, a fundamental procedure in docking investigations. This entails defining a three-dimensional grid encompassing the protein to map prospective ligand-binding regions. The grid facilitates systematic sampling of ligand poses and orientations during docking, thereby improving the precision of predicted protein–ligand associations in drug development pipelines. Within the Receptor Grid tool, the option to select ligand molecules was activated, followed by designation of the native ligand to centre the active site on its workspace centroid. The docking box dimensions ('dock ligand with length') were then resized to fully enclose the reference ligand [42, 43]. Subsequently, the Virtual Screening Workflow (VSW) tool, a widely utilised platform for tiered compound evaluation, was applied to perform multistage screening [42, 43]. The prepared SDF ligand library served as input, with Lipinski's rule enforced as a filter necessitating QikProp descriptor calculations [30, 44, 45]. Ligand preparation was bypassed since preprocessing had already been completed, and individual receptor grid files were manually assigned in the receptors panel. In the docking parameters, Epik state penalties were incorporated, and docking progressed through High Throughput Virtual Screening (HTVS), Standard Precision (SP), and Extra Precision (XP) protocols [36]. HTVS processed the full library, retaining only the top 10% for advancement to SP. Likewise, the leading 10% from SP proceeded to XP. In the XP phase, up to four poses were generated per ligand, and all XP-docked complexes were submitted for MM/GBSA rescoring using molecular mechanics with generalised Born surface area solvation [34, 46-51]. This cascaded filtering strategy optimised resource allocation by concentrating intensive calculations on high-potential hits. Upon completion, results were exported to CSV format for downstream analysis to determine drug-target interaction frequencies.

Molecular interaction fingerprints

Molecular Interaction Fingerprints (IFPs) constitute a cheminformatics technique that encodes ligand–environment contacts into a comparable binary or bit-string representation, capturing the presence of specific interaction types. The Interaction Fingerprints utility in Maestro was utilised to generate these profiles [30]. Receptor–ligand complexes were imported, all contact types were recorded, sequences were aligned to accommodate structural differences, and advanced options retained default values before fingerprint computation. In the resulting interaction matrix, contacts were visualised with colour coding in the primary plot, displaying only residues engaged in interactions. Additional panels depicted counts of ligand-centric and residue-centric interactions.

Pharmacokinetic and DFT studies

Pharmacokinetic evaluations investigate drug absorption, distribution, metabolism, and excretion profiles, elucidating bodily processing, bioavailability, metabolic pathways, and clearance rates. Such data inform dosing regimens to maximise safety and efficacy in clinical settings. Pharmacokinetic profiling of screened compounds was integrated via QikProp during virtual screening, with Lipinski's rule applied as a key filter—an integral component of the workflow [30, 44, 45]. Computed descriptors were benchmarked against established reference ranges. Density Functional Theory (DFT) geometry optimisation and property calculations were conducted using the Jaguar module within Maestro, leveraging quantum mechanical principles to refine structures and probe electronic characteristics [30, 52]. In drug discovery contexts, Jaguar enhances molecular model fidelity, providing insights into energetics and reactivity that bolster subsequent predictive computations [30, 53]. Input comprised the ligand structures, employing the B3LYP-D3 functional with a 6–31 G** basis set by default. The DFT method was specified in the theory panel, with automatic SCF spin multiplicity. Three-body dispersion correction was activated alongside compatible dispersion functionals. SCF accuracy was set to quick mode, starting from an atomic overlap initial guess. Convergence thresholds included a maximum of 48 iterations, energy variation of 5×10^{-5} Hartree, and RMS density matrix change of 5×10^{-6} [30, 52]. SCF acceleration utilised a 0 Hartree level shift, no thermal smearing, and the DIIS algorithm. Orbital consistency was enforced across isomers, using a single basis set without post-calculation localisation. Geometry optimisation allowed up to 100 steps, transitioning to analytic integrals near convergence, with default convergence criteria and an initial Schlegel Hessian in redundant internal coordinates. In the properties section, vibrational frequencies were calculated from the available Hessian, incorporating IR intensities and predominant isotopes; thermochemical data were generated at 1.0 atm and 298.15 K. Molecular surfaces were computed for electrostatic potential, average local ionisation energy, non-covalent interactions, electron density, spin density, HOMO, and LUMO, applying the PBF solvation model with water as solvent. Results were archived for review via the QM-Monitor interface [30, 52].

Molecular dynamics simulation's system preparation and production run

In this investigation, Desmond was utilised for molecular dynamics simulations to explore the interaction dynamics of IRESSA with breast cancer-associated proteins, yielding detailed information on protein–ligand contacts and revealing aspects of stability, flexibility, and intermolecular forces [33, 54]. This computational technique deepens our atomic-scale understanding of IRESSA's performance, guiding advancements in drug development [55]. The System Builder and Molecular Dynamics modules in computational chemistry are employed to assemble starting configurations for simulations and to execute production trajectories that model atomic motions over time [30, 54, 55]. Combined, they facilitate examination of dynamic properties in intricate biomolecular assemblies. The System Builder tool was applied to generate the simulation systems, incorporating the pre-defined SPC water model within an orthorhombic box with 10 × 10 × 10 Å buffer distances from the protein–ligand (P–L) complexes, ensuring appropriate enclosure [56]. Ion and salt placement was restricted outside a 20 Å radius. System neutrality was achieved by adding 2Cl− to the IRESSA–4KD7 complex, 6Na+ to the IRESSA–3RCD complex, 5Na+ to the IRESSA–1M17 complex, and 10Na+ to the IRESSA–5NWH complex. Box volume was further optimised to snugly accommodate each P–L complex. The OPLS4 force field was selected [38, 39], resulting in system sizes of 23,913 atoms for IRESSA–4KD7, 35,222 atoms for IRESSA–3RCD, 57,074 atoms for IRESSA–1M17, and 29,060 atoms for IRESSA–5NWH. The Molecular Dynamics panel was used to import the prepared systems, configuring a 100 ns simulation duration with trajectory recording every 100 ps and an energy recording interval of 1.2 ps, producing 1000 frames per run [30, 54, 55]. Simulations employed the NPT ensemble at 300 K and 1.01325 bar. Systems underwent relaxation prior to production, and resulting trajectories were analysed via the Simulation Interaction Diagram tool [30, 57].

Results and Discussion

Protein–ligand molecular interaction analysis

Computational docking of proteins and ligands predicts the binding configuration of a small-molecule candidate (ligand) to its macromolecular target through simulation. Its chief aim is to decipher affiliation patterns, thereby supporting the optimised creation of efficacious medicines. This method functions as an in silico iterative refinement, assessing diverse chemical entities' accommodation within protein cavities to pinpoint viable therapeutic contenders. Binding of the IRESSA molecule to Dihydrofolate reductase (PDB ID: 4KD7) achieved a docking score of −8.809 kcal/mol alongside an MM/GBSA value of −59.08 kcal/mol, facilitated through a hydrogen bond involving the ALA9 residue and the ligand's NH moiety **(Table 1, Figures 2Aa and 2Ab)**. The HER2 Kinase assembly (PDB ID: 3RCD) bound to IRESSA registered a docking score of −8.459 kcal/mol and MM/GBSA of −60.59 kcal/mol, incorporating a hydrogen bond from MET801 to a nitrogen atom plus a halogen interaction from ASP863 to the ligand's chlorine atom **(Table 1, Figures 2Ba and 2Bb).** Association of IRESSA with the epidermal growth factor receptor (PDB ID: 1M17) delivered a docking score of −9.021 kcal/mol and MM/GBSA of −61.74 kcal/mol, encompassing dual hydrogen bonds to MET769 (nitrogen) and ASP831 (protonated nitrogen), a salt bridge to ASP831 (protonated nitrogen), and a halogen contact to LEU764 (ligand chlorine) **(Table 1, Figures 2Ca and 2Cb).** Engagement of NUDT5 (PDB ID: 5NWH) with IRESSA gave a docking score of −4.527 kcal/mol and MM/GBSA of −49.09 kcal/mol, featuring dual hydrogen bonds to TYR90 (nitrogen) and PHE167 (ligand NH), complemented by dual pi–pi stacking from TYR90 to the ligand's aromatic rings **(Table 1, Figures 2Da and 2Db).**

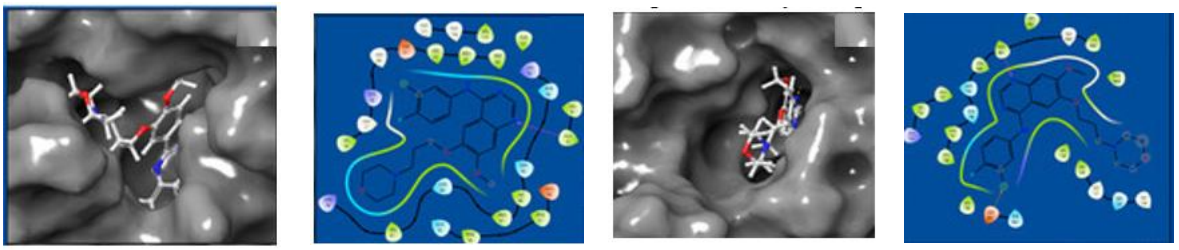

a b
A)

a b
B)

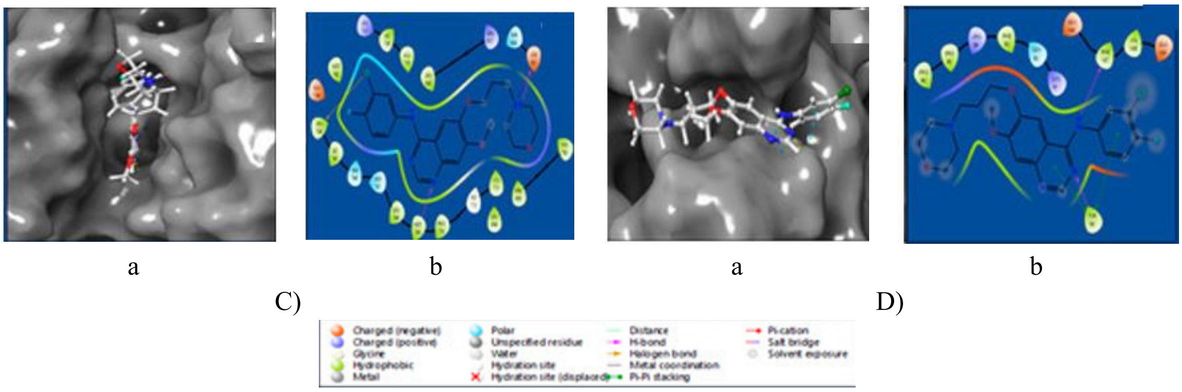

a b a b

C) D)

Figure 2. Illustrating interaction schematics between the proteins and IRESSA ligand, demonstrating site coverage alongside comprehensive perspectives: (Aa) 4KD7 three-dimensional, (Ab) 4KD7 two-dimensional, (Ba) 3RCD three-dimensional, (Bb) 3RCD two-dimensional, (Ca) 1M17 three-dimensional, (Cb) 1M17 two-dimensional, (Da) 5NWH three-dimensional, and (Db) 5NWH two-dimensional. An accompanying key explains residue categories and bond varieties.

Table 1. Displaying docking energies (kcal/mol), MM/GBSA energies (kcal/mol), and supplementary metrics for the interactions of all four targets with IRESSA.

S No	PDB ID	Docking Score	MMGBSA	Prime Hbond	Prime vdW	Ligand Efficiency ln	Ligand Efficiency sa
1	4KD7	−8.809	−59.08	−91.21	−897.44	−1.987	−0.893
2	3RCD	−8.459	−60.59	−152.23	−1316.69	−1.908	−0.857
3	1M17	−9.021	−61.74	−151.3	−1374.68	−2.035	−0.914
4	5NWH	−4.527	−49.09	−97.75	−703.04	−1.021	−0.459

Molecular Interaction Fingerprints

Molecular interaction fingerprinting represents a technique designed to examine the detailed contacts between a ligand and a target protein, generating a distinctive profile that highlights specific binding features. The IRESSA complexes formed with 4KD7, 3RCD, 1M17, and 5NWH exhibited numerous contacts contributing to their stability. The maximum (identical) number of interactions occurred in 4KD7 and 3RCD, followed by 1M17 in second place and 5NWH in third, based on the total count of ligand contacts **(Figure 3)**, (right side). The frequency of residue engagements with IRESSA is displayed on the upper portion of **Figure 3**, revealing the most frequently involved residues with the following occurrence counts: LEU (8), VAL (6), LYS (6), ASN (6), ILE (5), GLU (5), ARG (4), PRO (3), ASP (3), PHE (2), GLY (2), ALA (2), TYR (1), THR (1), SER (1), and GLN (1). Hydrophobic residues reduce solvent exposure to enhance complex stability, with Leucine (LEU) participating in eight interactions. Valine (VAL) and Isoleucine (ILE) also contribute notably, registering six and five contacts, respectively. Polar residues, capable of hydrogen bonding, bolster binding strength through Lysine (LYS) and Asparagine (ASN), each with six engagements, whereas Threonine (THR) and Serine (SER) each provide one. Charged residues drive electrostatic contributions essential for salt bridges and ionic contacts, prominently featuring Arginine (ARG) with four interactions and Aspartic acid (ASP) with three, the latter supporting both hydrogen bonds and salt bridges. Aromatic residues facilitate pi–pi stacking via Phenylalanine (PHE) and Tyrosine (TYR), each involved in two interactions with IRESSA's benzene rings. Compact residues like Alanine (ALA) and Glycine (GLY) deliver modest but significant roles, each with two contacts, aiding binding site adaptability. Proline (PRO) participates in three interactions, potentially shaping local pocket geometry and promoting overall complex integrity. Glutamic Acid (GLU) stands out with five interactions, leveraging its side chain for hydrogen bonds and salt bridges, demonstrating its multifunctional binding capacity. This in-depth evaluation deepens insight into the mechanistic foundation of IRESSA's polypharmacological profile, reinforcing its potential as a therapeutic option for breast cancer.

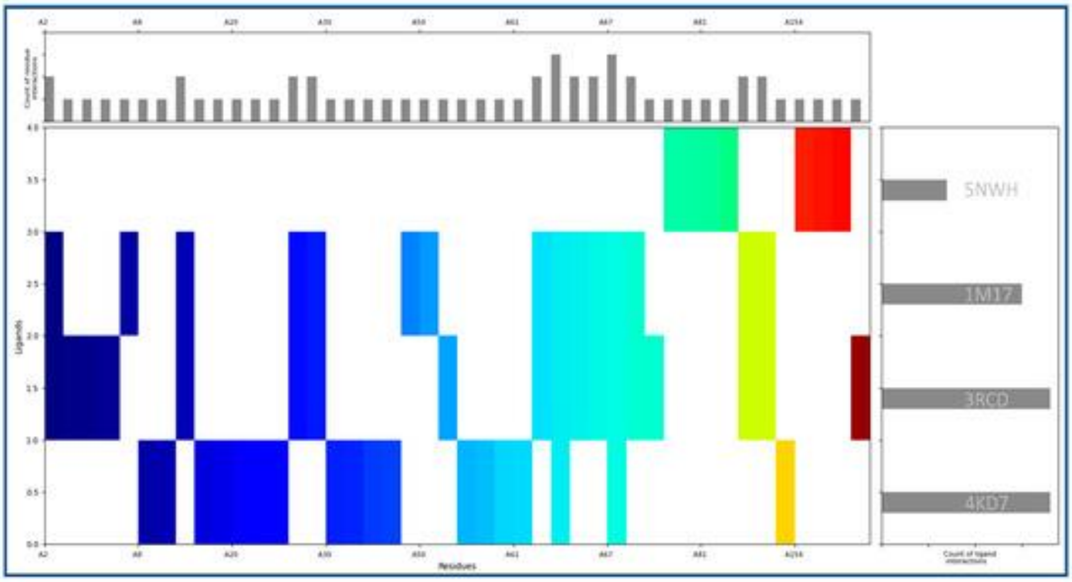

Figure 3. Illustrating the Molecular Interaction Fingerprinting of IRESSA across the four proteins. The coloured diagram depicts distributions of interacting residues, with the right-side panel indicating ligand interaction counts and the upper panel showing residue interaction frequencies, facilitating identification of dominant residue–ligand pairings.

DFT and pharmacokinetic studies

In this thorough examination of IRESSA as a potential therapeutic agent, we applied the TDDFT(b3lyp-d3)/SOLV approach using a 6–31 g** basis set, yielding an extensive array of molecular descriptors that illuminate key physicochemical attributes. The total count of canonical orbitals, fundamental to electronic configuration analysis, stood at 587. Geometry optimisation achieved a convergence level classified as four, reflecting high structural refinement accuracy. Energy assessments revealed a gas-phase ground state energy of −1857.538131 and a marginally stabilised solution-phase value of −1857.5665. The computed solvation energy, indicative of environmental adaptability, amounted to −17.801717 kcal/mol. Electronic properties were extensively characterised, particularly through HOMO and LUMO energies, which inform reactivity and stability, alongside data on the lowest singlet excitation and corresponding oscillator strength.

To explore IRESSA's spectroscopic behaviour, three-dimensional dipole moment components (X, Y, and Z) were evaluated, shedding light on molecular polarity. Electrostatic potential (ESP) metrics—including minimum, maximum, average values, and variance—were carefully assessed to elucidate intermolecular interaction tendencies. Likewise, Average Local Ionisation Energy (ALIE) descriptors, covering minimum, maximum, mean, and balance parameters, together with the Average Absolute Deviation from the Mean ALIE, offered valuable perspectives on regional reactivity and ionisation uniformity. Graphical depictions in **Figure 4** illustrated various energy landscapes, enhancing comprehension of IRESSA's structural and energetic features. **Figure 5** presented core molecular visualisations, encompassing electron density, electrostatic potential, HOMO, and LUMO distributions, providing essential guidance for subsequent optimisation in drug development.

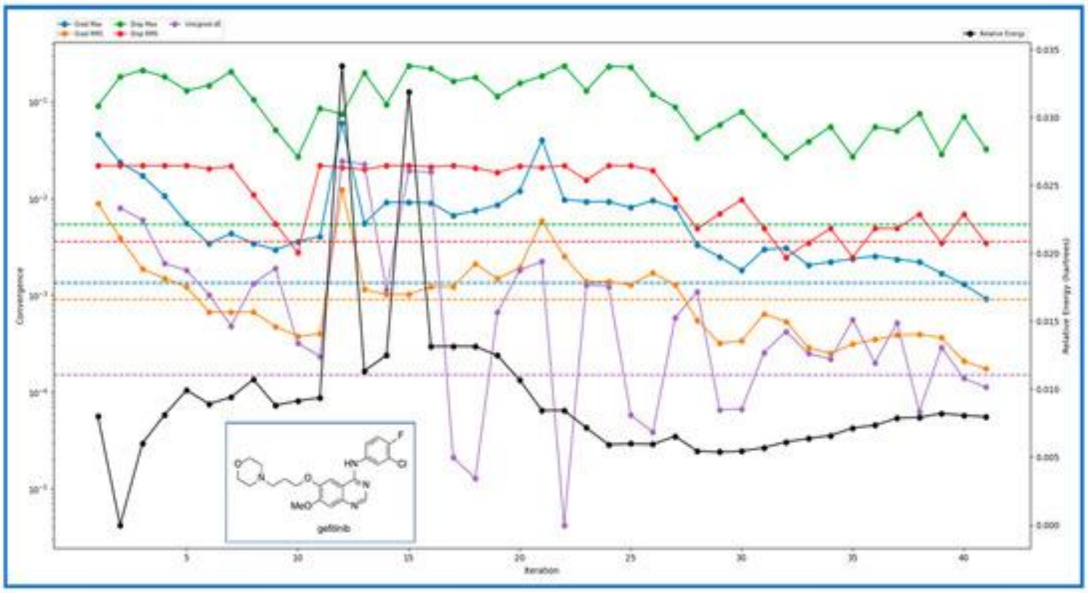

Figure 4. Illustrating the various energy levels obtained following multiple optimisation iterations across time, alongside comparisons to the relative energy states of the compounds. The Grad Max is depicted in blue, Disp Max in green, Grad RMS in orange, and Disp RMS in red. Unsigned dE appears in magenta, whereas the relative energy (in Hartree units) is represented in black.

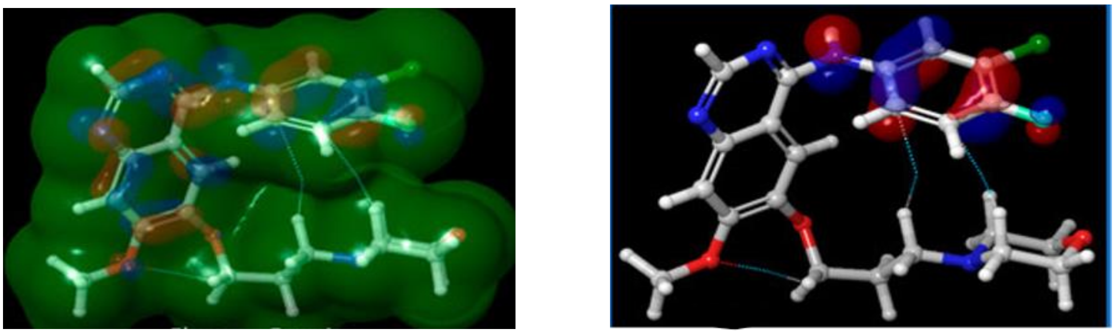

electron density HOMO

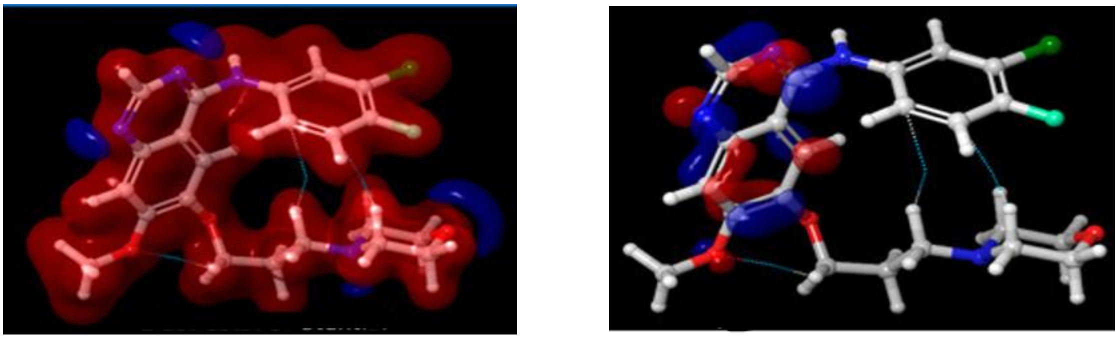

electrostatic potential LUMO

Figure 5. Depicting the distinct energy profiles of the IRESSA compound. Representations include electron density, electrostatic potential, as well as the HOMO and LUMO regions, to elucidate the molecule's energy distribution at both lower and higher orbitals.

Assessment of IRESSA via QikProp involved examining multiple descriptors and derived parameters against established benchmark values, yielding key information on its drug-like attributes. IRESSA displayed zero acidic or amidine functionalities, complying with the recommended limit of 0–1 for each. It possessed one amine group, also within the permitted 0–1 range. The molecule incorporated 22 out of 56 atoms, reflecting appropriate structural complexity. Predictions for metabolic sites numbered five, situated comfortably in the 1–8 acceptable window. The count of nitrogen and oxygen atoms reached 7, consistent with the standard interval of 2–15 (**Table**

2). For lipophilicity and permeability, the QPlogPw registered 10.783, inside the 4.0–45.0 bounds. The polar surface area (PSA) measured 61.141, well within the 7.0–200.0 guideline, signalling advantageous polarity. Human oral absorption proved outstanding, achieving a PercentHumanOralAbsorption of 100%, exceeding the high-absorption benchmark of >80%. On safety aspects, QikProp highlighted a potential issue with QPlogHERG at −7.087, falling below the −5 concern threshold **(Table 2).** The QPlogKhsa of 0.349 remained within the −1.5 to 1.5 range, indicating suitable human serum albumin binding. IRESSA conformed to both Lipinski's Rule of Five and Rule of Three, presenting a QPlogBB of 0.312 and QPlogPo/w of 4.31. Additional physicochemical metrics—including SAfluorine, SASA, volume, and WPSA—aligned with recommended limits, supporting strong drug-like potential **(Table 2).** Overall, the QikProp analysis revealed that IRESSA exhibits favourable pharmacokinetic characteristics in line with conventional drug development criteria, reinforcing its candidacy as a viable and potentially safe therapeutic agent.

Table 2. Presenting the ADMET profile of the IRESSA compound alongside comparisons to QikProp reference standards.

Descriptor	Iressa Value	Standard/Acceptable Range	Descriptor	Iressa Value	Standard/Acceptable Range
Number of carboxylic acids	0	0–1	Human Oral Absorption	3	-
Number of amides	0	0–1	Ionization Potential (eV)	8.475	7.9–10.5
Number of amidines	0	0	Apparent MDCK permeability	0.007	-
Number of amines	1	0–1	Molecular Weight	446.908	130.0–725.0
Atoms in 3- or 4-membered rings	0	-	Percent Human Oral Absorption	100	>80% high, <25% poor
Atoms in 5- or 6-membered rings	22	-	Pi (hydrophobic) Surface Area	242.502	0.0–450.0
Predicted metabolic reactions	5	1–8	Polar Surface Area	61.141	7.0–200.0
Number of nitrogen and oxygen atoms	7	2–15	Brain/Blood Partition Coefficient	0.312	−3.0–1.2
Number of non-conjugated bonds	4	-	hERG K+ channel blockage (logIC50)	−7.087	concern below −5
Number of non-hydrogen atoms	31	-	Human serum albumin binding	0.349	−1.5–1.5
Number of atoms in aromatic rings	22	-	Skin permeability (log Kp)	−2.682	−8.0–−1.0
Number of rotatable bonds	8	0–15	Hexadecane/gas partition coeff.	13.202	4.0–18.0
Reactive functional groups	0	0–2	Octanol/Water partition coeff.	4.31	−2.0–6.5
Drug-likeness penalty stars	0	0–5	Octanol/gas partition coeff.	20.444	8.0–35.0
Hydrogen bond acceptors (estimated)	7.7	2.0–20.0	Water/gas partition coeff.	10.783	4.0–45.0
(ACxDN^0.5)/SA index	0.0101519	0.0–0.05	Predicted aqueous solubility (log S)	−5.129	−6.5–0.5
Category	small	-	Caco-2 cell permeability	1049.999	<25 poor, >500 excellent
Conformation-independent QPlogS	−5.22	−6.5–0.5	MDCK cell permeability	2306.642	<25 poor, >500 excellent

CNS activity (predicted)	1	−2 (inactive), +2 (active)	Polarizability	44.448	13.0–70.0
(Dipole moment)^2 / Volume	0.0220798	0.0–0.13	Rule of Five violations	0	maximum 4
Dipole moment	5.429	1.0–12.5	Rule of Three violations	0	maximum 3
Hydrogen bond donors	1	0.0–6.0	Amide oxygen surface area	0	0.0–35.0
Electron affinity (eV)	1.279	−0.9–1.7	Fluorine surface area	41.345	0.0–100.0
Hydrophilic surface area	39.187	7.0–330.0	Total solvent-accessible surface area	758.477	300.0–1000.0
Hydrophobic surface area	366.922	0.0–750.0	Molecular volume	1334.913	500.0–2000.0
Globularity	0.7730209	0.75–0.95	Weakly polar surface area	109.866	0.0–175.0

Molecular dynamics simulations

Molecular dynamics (MD) simulations track the time-dependent motion of molecular systems by numerically integrating Newton's equations of motion, enabling analysis of atomic trajectories and interactions that reveal dynamic properties, including positional deviations, flexibility fluctuations, and intermolecular forces. Root-mean-square deviation (RMSD) quantifies the mean displacement of atoms relative to a starting or reference conformation, serving as an indicator of overall structural integrity. In contrast, root-mean-square fluctuation (RMSF) evaluates the mobility of specific residues or atoms across the simulation timeframe. Intermolecular interactions encompass contributions from van der Waals contacts, hydrogen bonds, and electrostatic forces, collectively governing the system's stability and conformational behaviour throughout the MD trajectory.

Root mean square deviation

Root Mean Square Deviation (RMSD) is a fundamental tool in computational structural biology for gauging the typical shift in atomic positions away from a reference frame during molecular dynamics runs or when superimposing structures. It offers a numerical summary of overall conformational differences between coordinate sets, commonly used to benchmark simulated models against experimental ones. Smaller RMSD figures reflect closer structural alignment and greater persistence of the initial fold. Computation requires optimal superposition of the two structures followed by taking the square root of the averaged squared distances between corresponding atoms, yielding an objective measure of either predictive accuracy or temporal robustness in simulations. In the IRESSA-bound Dihydrofolate reductase (PDB ID: 4KD7), the protein started with a deviation of 0.77 Å, the ligand reached 0.42 Å by 0.10 ns, and by the end of 100 ns the values stood at 2.19 Å for the protein and 2.52 Å for the ligand—entirely within tolerable limits for biomolecular systems and effectively under 2 Å on average **(Figure 6a)**. For the HER2 Kinase–IRESSA assembly (PDB ID: 3RCD), early protein deviation was 1.17 Å with the ligand at 1.77 Å after 0.10 ns; by 100 ns these rose to 2.73 Å (protein) and 1.99 Å (ligand), demonstrating consistently reliable stability throughout **(Figure 6b)**. The epidermal growth factor receptor complexed with IRESSA (PDB ID: 1M17) opened with 2.01 Å protein deviation and 1.43 Å for the ligand at 0.10 ns; the subsequent trajectory proved steady, concluding at 5.49 Å (protein) and 3.02 Å (ligand) after 100 ns, with deviations falling into acceptable ranges once the initial 1 ns equilibration period is excluded **(Figure 6c).** The NUDT5–IRESSA pairing (PDB ID: 5NWH) began at 1.83 Å for the protein and moved to 2.05 Å for the ligand by 0.10 ns, eventually reaching 6.87 Å (protein) and 19 Å (ligand) at 100 ns—a notably larger excursion (**Figure 6d**). These trajectory details deepen our appreciation of how IRESSA maintains binding integrity across diverse breast cancer targets. Plots distinguish Cα traces in blue, full backbone in green, and ligand in red.

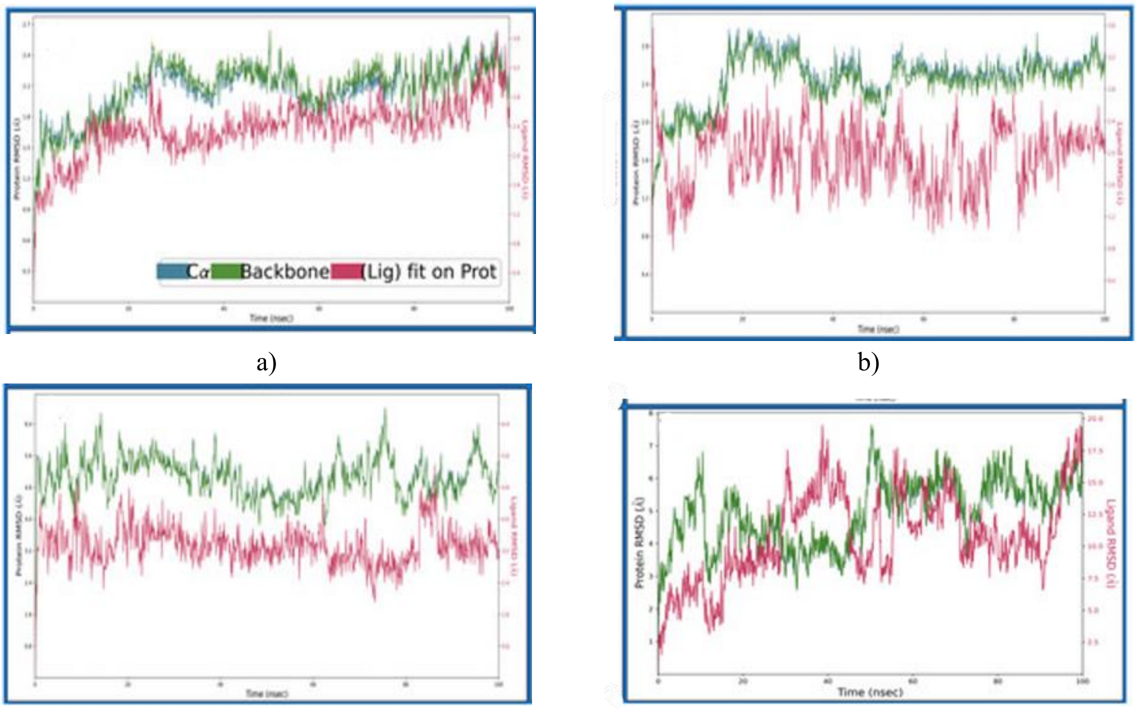

a) b)

c) d)

Figure 6. Displaying Root Mean Square Deviation (RMSD) profiles for IRESSA (red) against Cα (blue) and backbone (army green) atoms in the protein complexes (a) 4KD7, (b) 3RCD, (c) 1M17, and (d) 5NWH across the 100 ns molecular dynamics simulation.

Root mean square fluctuations

Root Mean Square Fluctuation (RMSF) quantifies the mobility of specific atoms or residues in a biomolecule over the course of a molecular dynamics simulation by measuring their variance from the time-averaged position. It highlights regions of high flexibility versus rigidity within the structure. The 4KD7–IRESSA system revealed several residues exceeding 2 Å fluctuation: VAL1, GLY2, ASN19, PRO103, GLU104, GLU154, GLY164, SER167, and ASP186. A substantial number of residues formed stabilising contacts with IRESSA, namely ILE7, VAL8, ALA9, ILE16, ASN19, GLY20, LEU22, GLU30, PHE31, TYR33, PHE34, GLN35, MET52, LYS55, THR56, SER59, ILE60, PRO61, LYS63, ASN64, PRO66, LEU67, ARG70, VAL115, SER118, TYR121, and THR146 **(Figure 7a)**. In the 3RCD–IRESSA complex, residues showing >2 Å mobility included ALA710, ASN745, SER792, GLU876-LYS883, GLN990-PRO999, ASP1011, ASP1013, and VAL1018-GLU1022; residues contributing to complex integrity through ligand contacts were LEU726, SER728, ALA730, PHE731, VAL734, ALA751, LYS753, SER783, LEU785, THR798, LEU800, MET801, CYS805, LEU807, ASP808, ARG811, ASP845, ARG849, ASN850, LEU852, THR862, ASP863, GLY881, PHE1004, and LEU1008 **(Figure 7b).** For the 1M17–IRESSA assembly, highly mobile segments (>2 Å) encompassed GLY672-ALA678, GLY711-LYS713, GLU725-LYS730, SER760, HIS781-GLY786, ALA840, GLU841, ALA847-GLY850, HIS864, ARG865, GLY893, PRO895, SER897, GLU898, SER901, GLU904, LYS905, PRO913, ILE914, ARG949, ASP950, GLN952, ARG953, and VAL956-PRO995; stabilising interactions originated from LYS692, LEU694, SER696, PHE699, VAL702, ALA719, LYS721, CYS751, THR766, LEU768, MET769, CYS773, ASP776, ARG779, GLU780, ARG817, LEU820, THR830, and ASP831 **(Figure 7c).** The 5NWH–IRESSA complex featured elevated mobility (>2 Å) in LYS14-THR58, THR71, LEU72, ARG84-GLY89, ASP133-ASN138, ALA153, GLU154, ALA156, ARG157, PRO162-PHE167, ASP183, ALA184, VAL186-HIS190, and LEU202-ASN208; residues anchoring the ligand included GLU25, GLY26, LYS27, TRP28, VAL29, LYS33, LYS42, THR45, TRP46, GLU47, LYS81, GLN82, PHE83, ARG84, PRO85, PRO86, MET87, GLY88, TYR90, LYS161, PRO162, ASP164, GLU166, PHE167, VAL168, GLU169, GLU188, GLU189, HIS190, and THR192 **(Figure 7d).**

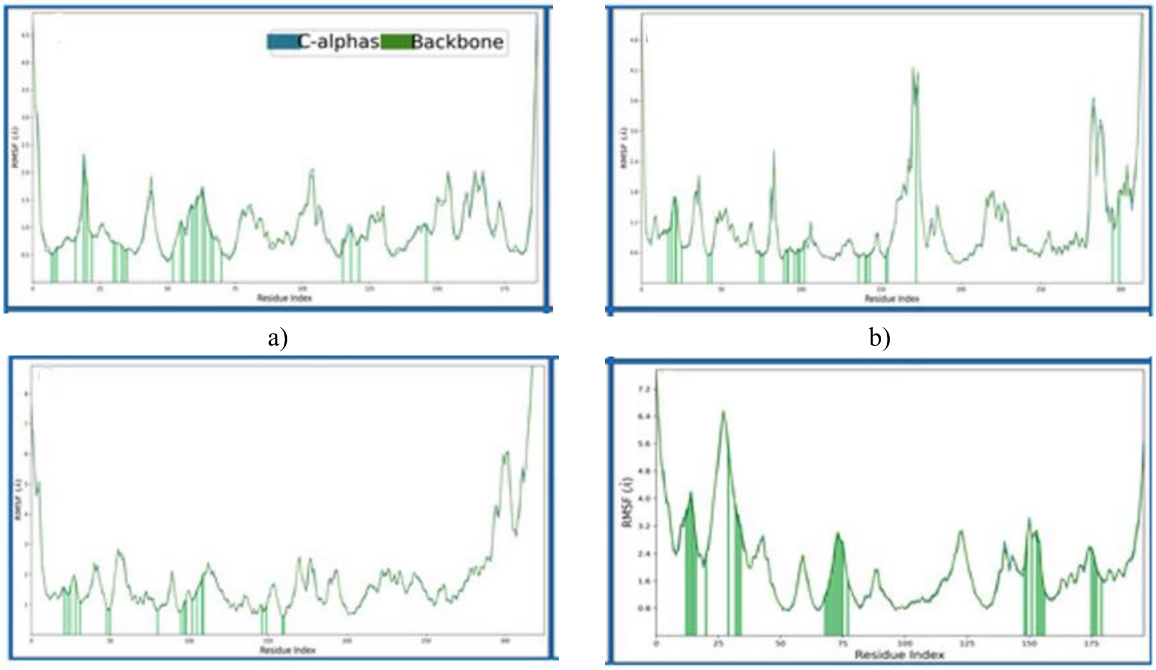

a) b) c) d)

Figure 7. Presenting Root Mean Square Fluctuation (RMSF) values for Cα (blue) and backbone (army green) atoms across the proteins (a) 4KD7, (b) 3RCD, (c) 1M17, and (d) 5NWH. Green vertical lines mark residues engaged in ligand contacts during the 100 ns molecular dynamics run.

Simulation interaction diagrams

Intermolecular forces dictate the associations between distinct molecules, profoundly affecting their characteristics and behaviour. Van der Waals attractions arise from transient dipoles, encompassing dispersion forces and permanent dipole interactions. Hydrogen bonds represent a stronger subset of dipole interactions, occurring when hydrogen atoms link to highly electronegative elements. Ionic bonds stem from electrostatic pull between oppositely charged species, whereas hydrophobic effects drive non-polar groups to aggregate away from aqueous surroundings. Grasping these forces is essential across chemistry, biology, and materials disciplines, as they illuminate molecular-level phenomena and material attributes. In the IRESSA-bound Dihydrofolate reductase (PDB ID: 4KD7), numerous hydrogen bonds formed involving GLY20 and SER59 with water and a ligand NH group, ASN64, GLY20, and ILE16 with water, ALA9 with three ligand nitrogen atoms, and GLU30 plus ASN64 with water bridging three oxygen atoms; additionally, pi–pi stacking occurred between TYR121 and a benzene ring of IRESSA **(Figure 8a).** The HER2 Kinase–IRESSA complex (PDB ID: 3RCD) featured multiple hydrogen bonds, including ASP863 with water and a ligand NH, THR798, THR862, ASP808, and ARG849 with water, MET801 with three ligand nitrogens, and CYS805, LEU726, SER728, plus ASP808 with water across three oxygens; a pi-cation interaction also linked LYS753 to a ligand benzene ring **(Figure 8b).** For the epidermal growth factor receptor paired with IRESSA (PDB ID: 1M17), eight water molecules acted as bridges enhancing stability, alongside hydrogen bonds from ASP776 to a protonated ligand nitrogen, ASP831 via water to a ligand NH, MET768, THR830, and THR766 with water mediating two ligand nitrogens, and ASP776 plus CYS773 with two ligand oxygens; a salt bridge further connected ASP776 to the ligand's protonated nitrogen **(Figure 8c).** The NUDT5–IRESSA assembly (PDB ID: 5NWH) displayed hydrogen bonds involving GLY88 with a ligand NH and VAL168, TYR90, plus GLU169 with water bridging two ligand nitrogens, complemented by seven pi–pi stacking contacts from TYR90, PHE83, HIS190, and PHE167 to three benzene rings of IRESSA **(Figure 8d).** Ligand-contacting residues are highlighted in green for clarity on binding sites, with backbone traces compared to Cα fluctuations for deeper insight. Interaction frequencies are summarised in **Figure 9**, presented as histograms categorising H-bonds, hydrophobic contacts, ionic bonds, and water bridges.

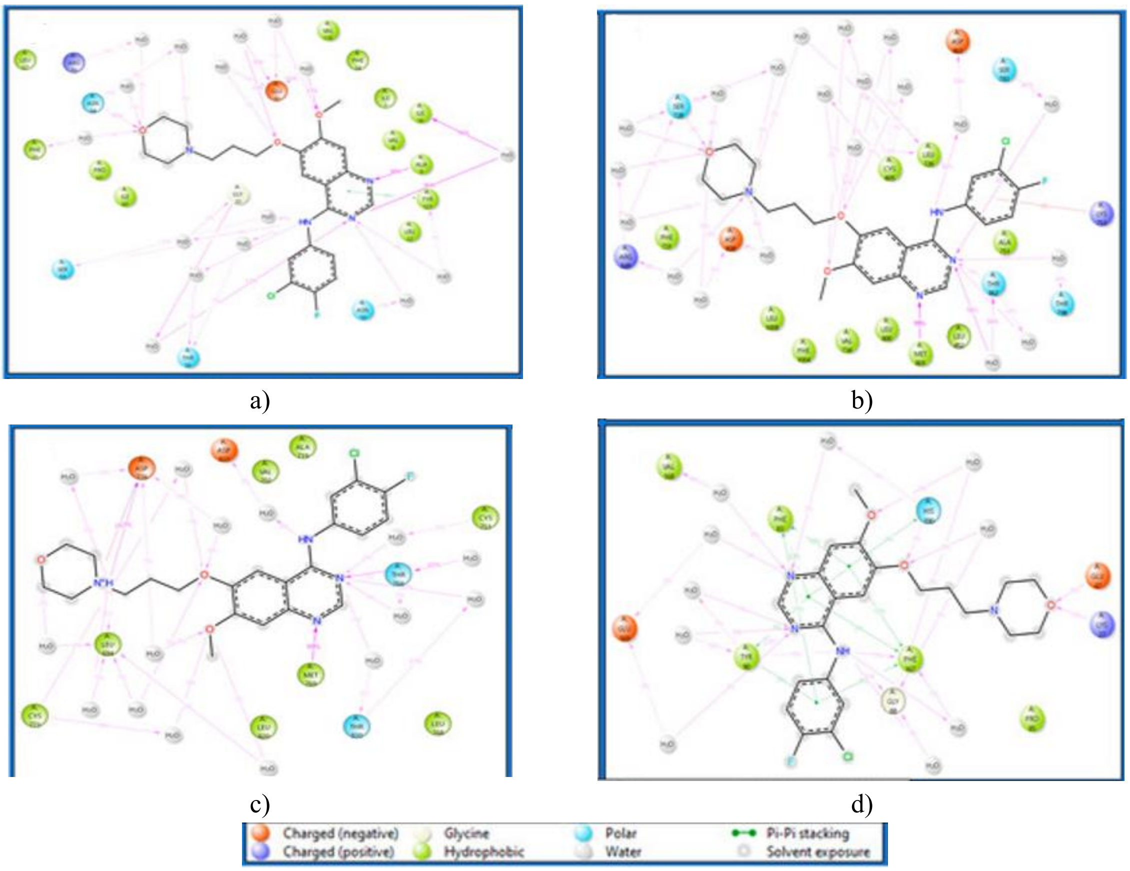

a)

b)

c)

d)

Figure 8. Depicting the simulation interaction profiles for IRESSA within complexes of (a) 4KD7, (b) 3RCD, (c) 1M17, and (d) 5NWH. A legend accompanies the diagrams to clarify interaction categories and bond classifications.

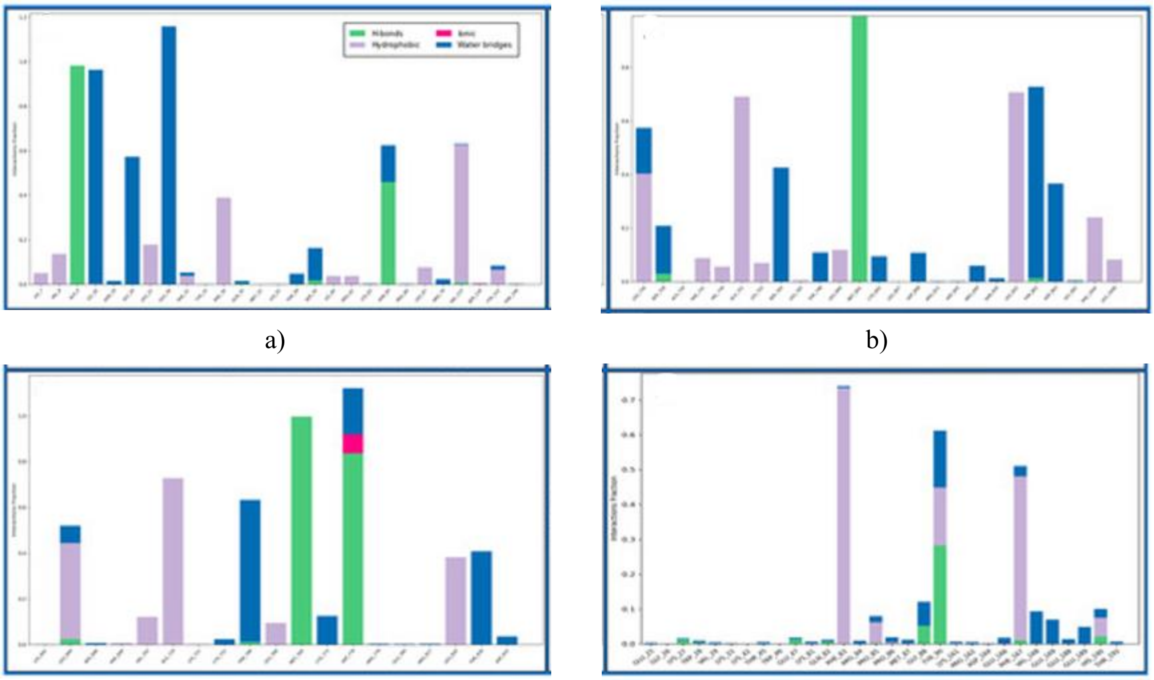

a)

b)

c)

d)

Figure 9. Quantifying interactions from the simulation diagrams of IRESSA across complexes with (a) 4KD7, (b) 3RCD, (c) 1M17, and (d) 5NWH, with H-bonds in green, ionic in red, hydrophobic in grey, and water bridges in blue.

The findings from our in-depth investigation position IRESSA as a strong candidate for multitargeted therapy in breast cancer. Our work commenced with protein–ligand docking simulations to elucidate the detailed binding modes of IRESSA with critical breast cancer-related proteins: Dihydrofolate reductase (PDB ID: 4KD7), HER2 Kinase (PDB ID: 3RCD), epidermal growth factor receptor (PDB ID: 1M17), and NUDT5 (PDB ID: 5NWH). Docking scores and MM/GBSA energies proved essential for evaluating binding strength and complex durability. IRESSA exhibited potent engagements through hydrogen bonds, halogen bonds, and salt bridges, resulting in robust complexes with these targets. These binding patterns are visually captured in **Figure 2**, highlighting key participating residues and confirming overall complex integrity. Additional understanding of interaction profiles emerged from molecular interaction fingerprinting, which mapped ligand contact distributions and identified the most frequently engaged residues. Diverse amino acid classes coordinate a network of stabilising contributions that dictate IRESSA's attachment to pivotal breast cancer proteins **(Figure 3)**. Leading the hydrophobic contributions, Leucine (LEU) registered eight contacts, supported by Valine (VAL) with six and Isoleucine (ILE) with five, together creating a non-polar core that shields the complex from solvent and bolsters stability. Polar amino acids, notably Lysine (LYS) and Asparagine (ASN), each with six engagements, are central to hydrogen bond formation, thereby strengthening affinity. Charged groups, headed by Arginine (ARG) at four interactions and Aspartic Acid (ASP) at three, harness electrostatic forces to generate salt bridges and ionic contacts, introducing further sophistication. Aromatic side chains from Phenylalanine (PHE) and Tyrosine (TYR), each contributing two contacts, facilitate pi–pi stacking against IRESSA's aromatic rings. Compact residues such as Alanine (ALA) and Glycine (GLY), both with two interactions, modestly enhance pocket flexibility and accommodation. Proline (PRO), owing to its conformational constraints, engages in three contacts that may shape local geometry. Glutamic Acid (GLU), with five interactions, demonstrates broad utility by mediating both hydrogen bonds and salt bridges. This elaborate orchestration of residue contributions deepens insight into IRESSA's binding rationale and underscores its promise as a polypharmacological agent against breast cancer.

The thorough examination presented in **Figure 4** illuminates IRESSA's consistent performance across varied targets. Quantum chemical calculations, conducted via the TDDFT(b3lyp-d3)/SOLV approach with a 6–31 g** basis set, probed the molecule's electronic framework and energetic profile. A wide array of descriptors—from canonical orbital count to solvation energy—delivered a detailed portrait of its properties. **Figure 4** consolidates these outcomes, revealing the nuanced molecular characteristics of IRESSA. Drug-likeness assessment was advanced through QikProp evaluation, encompassing numerous descriptors benchmarked against reference standards. Critical attributes related to lipophilicity, permeability, and toxicity flags were inspected. Overall, IRESSA displayed favourable pharmacokinetic traits conforming to conventional drug development criteria. These data, summarised in **Table 2,** affirm its viability as a potent and tolerable therapeutic prospect.

Our investigation extended into molecular dynamics (MD) simulations, which capture the time-evolving behaviour of molecules and yield detailed perspectives on IRESSA's conformational stability and flexibility. Analyses of Root Mean Square Deviation (RMSD) and Root Mean Square Fluctuation (RMSF) delivered numerical evaluations of structural shifts and regional mobility, respectively. As shown in **Figures 6 and 7**, the trajectories revealed stable IRESSA complexes characterised by tolerable deviations and confined fluctuations. The Simulation Interaction Diagrams presented in **Figure 8** deepened this insight by dissecting the operative intermolecular contacts. Specific details on hydrogen bonds, pi–pi stacking, and water-mediated bridges furnished a fine-grained view of the factors sustaining complex integrity. A quantitative summary of interaction frequencies appeared in **Figure 9**, highlighting the dominance of hydrogen bonds, hydrophobic contacts, ionic bonds, and water bridges.

Alignment with current advances in breast cancer drug discovery reinforces that IRESSA embodies modern polypharmacology principles. Its diverse engagements with breast cancer-associated proteins, combined with advantageous physicochemical attributes, establish it as an attractive multitargeted therapeutic prospect. The orchestrated interplay of molecular forces uncovered here adds refined contributions to the progressing field of breast cancer treatment strategies.

In summary, IRESSA stands out from this work as a versatile and encouraging candidate for breast cancer management. Integration of computational docking, quantum mechanical calculations, and molecular dynamics simulations yields a comprehensive molecular-level portrait of its performance [58-60]. These outcomes not only expand understanding of IRESSA but also enrich the wider conversation on drug design and development, particularly for breast cancer where precise and potent interventions remain critically needed. IRESSA, originally designed as an epidermal growth factor receptor (EGFR) tyrosine kinase inhibitor for lung cancer, has attracted interest for possible applications in breast cancer [58-60]. Overactivation of EGFR can drive tumour cell proliferation, and evidence indicates potential activity of IRESSA against certain breast cancer subtypes with elevated EGFR expression. Nevertheless, its utility in breast cancer is far less consolidated than in lung cancer, where it benefits from broader clinical validation and routine application [58-60]. As with all oncological agents, any consideration of IRESSA for breast cancer must involve thorough discussion with oncology specialists, accounting for tumour characteristics, patient health status, and alternative therapies. Remaining current with emerging research and seeking tailored guidance from healthcare providers is essential.

This investigation delivers an extensive appraisal of IRESSA as a prospective multitargeted agent against breast cancer, leveraging an integrated suite of computational modelling, quantum chemistry, and molecular dynamics approaches. The granular revelations concerning protein–ligand binding, molecular descriptors, and complex durability supply meaningful data supporting its therapeutic promise. To propel IRESSA’s evaluation forward, progression from virtual screening to preclinical in vivo experiments and subsequent clinical trials is vital for realistic appraisal of efficacy and tolerability. Investigating synergistic regimens, elucidating resistance pathways, and pinpointing predictive biomarkers for patient selection represent key avenues for refinement. Moreover, prolonging molecular dynamics trajectories to support pharmacological profiling could bolster the robustness and translational relevance of the results. Incorporation of patient-derived xenografts or organoids, alongside vigilant tracking of advancing literature in breast cancer therapeutics and drug innovation, will be instrumental in sharpening IRESSA’s position within personalised treatment paradigms. Ultimately, the present work establishes a solid platform for viewing IRESSA as a polyvalent candidate, while the proposed next steps seek to translate in silico forecasts into clinical realities, advancing the pipeline of targeted breast cancer interventions.

Conclusion

Breast cancer continues to pose a major worldwide health burden, affecting millions of women across the globe. This work underscores the intricate issue of drug resistance in breast cancer management, highlighting the urgency for novel therapeutic approaches. Through multitargeted virtual screening, IRESSA emerged as an encouraging inhibitor of key oncogenic proteins. Analyses involving interaction fingerprints, DFT calculations, ADMET profiling, and molecular dynamics simulations confirmed its binding stability, indicating prospective therapeutic potential. Although IRESSA holds FDA approval for lung cancer, its polypharmacological profile supports exploration of repurposing for breast cancer applications. Empirical validation remains essential to establish its efficacy, yet these computational insights provide an optimistic pathway for subsequent investigations aimed at overcoming resistance mechanisms in breast cancer.

Acknowledgments: None

Conflict of Interest: None

Financial Support: None

Ethics Statement: None

References

1. Feng, Y.; Spezia, M.; Huang, S.; Yuan, C.; Zeng, Z.; Zhang, L.; Ji, X.; Liu, W.; Huang, B.; Luo, W.; et al. Breast cancer development and progression: Risk factors, cancer stem cells, signaling pathways, genomics, and molecular pathogenesis. *Genes Dis.* **2018**, *5*, 77–106.
2. Manoharan, S.; Pugalendhi, P. Breast Cancer: An Overview. *J. Cell Tissue Res.* **2010**, *10*, 2423–2432.
3. Russo, J.; Hu, Y.F.; Silva, I.D.; Russo, I.H. Cancer risk related to mammary gland structure and development. *Microsc. Res. Tech.* **2001**, *52*, 204–223.
4. Karwasra, R.; Ahmad, S.; Bano, N.; Qazi, S.; Raza, K.; Singh, S.; Varma, S. Macrophage-targeted punicalagin nanoengineering to alleviate methotrexate-induced neutropenia: A molecular docking, DFT, and MD simulation analysis. *Molecules* **2022**, *27*, 6034.
5. Karwasra, R.; Khanna, K.; Singh, S.; Ahmad, S.; Verma, S. *Computational Intelligence in Oncology*; Springer: Berlin/Heidelberg, Germany, 2022; Volume 1016, pp. 369–384.

6. Kaul, T.; Eswaran, M.; Ahmad, S.; Thangaraj, A.; Jain, R.; Kaul, R.; Raman, N.M.; Bharti, J. Probing the effect of a plus 1bp frameshift mutation in protein-DNA interface of domestication gene, NAMB1, in wheat. *J. Biomol. Struct. Dyn.* **2019**, *38*, 3633–3647.
7. Khuntia, B.K.; Sharma, V.; Wadhawan, M.; Chhabra, V.; Kidambi, B.; Rathore, S.; Sharma, G. Antiviral potential of Indian medicinal plants against influenza and SARS-CoV: A systematic review. *Nat. Prod. Commun.* **2022**, *17*, 1934578X221086988.
8. Rana, M.; Ahmedi, S.; Fatima, A.; Ahmad, S.; Nouman; Siddiqui, N.; Raza, K.; Manzoor, N.; Javed, S. Synthesis, single crystal, TD-DFT, molecular dynamics simulation and DNA binding studies of carbothioamide analog. *J. Mol. Struct.* **2023**, *1287*, 135701.
9. Hooley, R.J.; Scoutt, L.M.; Philpotts, L.E. Breast ultrasonography: State of the art. *Radiology* **2013**, *268*, 642–659.
10. Sathish, D.; Kamath, S.; Rajagopal, K.; Prasad, K. Medical imaging techniques and computer aided diagnostic approaches for the detection of breast cancer with an emphasis on thermography-a review. *Int. J. Med. Eng. Inform.* **2016**, *8*, 275–299.
11. Olopade, O.I.; Grushko, T.A.; Nanda, R.; Huo, D. Advances in breast cancer: Pathways to personalized medicine. *Clin. Cancer Res.* **2008**, *14*, 7988–7999.
12. Cherny, N.I.; Paluch-Shimon, S.; Berner-Wygoda, Y. Palliative care: Needs of advanced breast cancer patients. *Breast Cancer Targets Ther.* **2018**, *10*, 231–243.
13. Stamos, J.; Sliwkowski, M.X.; Eigenbrot, C. Structure of the epidermal growth factor receptor kinase domain alone and in complex with a 4-anilinoquinazoline inhibitor. *J. Biol. Chem.* **2002**, *277*, 46265–46272.
14. Ishikawa, T.; Seto, M.; Banno, H.; Kawakita, Y.; Oorui, M.; Taniguchi, T.; Kamiyama, K. Design and synthesis of novel human epidermal growth factor receptor 2 (HER2)/epidermal growth factor receptor (EGFR) dual inhibitors bearing a pyrrolo [3, 2-d] pyrimidine scaffold. *J. Med. Chem.* **2011**, *54*, 8030–8050.
15. Page, B.D.; Valerie, N.C.K.; Wright, R.H.G.; Wallner, O.; Isaksson, R.; Carter, M.; Rudd, S.G.; Loseva, O.; Jemth, A.-S.; Almlöf, I.; et al. Targeted NUDT5 inhibitors block hormone signaling in breast cancer cells. *Nat. Commun.* **2018**, *9*, 250.
16. Lamb, K.M.; G-Dayanandan, N.; Wright, D.L.; Anderson, A.C. Elucidating features that drive the design of selective antifolates using crystal structures of human dihydrofolate reductase. *Biochemistry* **2013**, *52*, 7318–7326.
17. Rana, M.; Hungyo, H.; Parashar, P.; Ahmad, S.; Mehandi, R.; Tandon, V.; El-Bahy, Z.M. Design, synthesis, X-ray crystal structures, anticancer, DNA binding, and molecular modelling studies of pyrazole–pyrazoline hybrid derivatives. *RSC Adv.* **2023**, *13*, 26766–26779.
18. Sahu, A.; Ahmad, S.; Imtiyaz, K.; Kumaran, A.K.; Islam, M.; Raza, K.; Easwaran, M.; Kunnath, A.K.; Rizvi, M.A.; Verma, S. In-silico and in-vitro study reveals Ziprasidone as a potential aromatase inhibitor against breast carcinoma. *Sci. Rep.* **2023**, *13*, 16545.
19. Shah, A.A.; Ahmad, S.; Yadav, M.K.; Raza, K.; Kamal, M.A.; Akhtar, S. Structure-based virtual screening, molecular docking, molecular dynamics simulation, and metabolic reactivity studies of quinazoline derivatives for their anti-EGFR activity against tumor angiogenesis. *Curr. Med. Chem.* **2023**, *31*, 595–619.
20. Singh, A.P.; Ahmad, S.; Raza, K.; Gautam, H.K. Computational screening and MM/GBSA-based MD simulation studies reveal the high binding potential of FDA-approved drugs against *Cutibacterium acnes* sialidase. *J. Biomol. Struct. Dyn.* **2023**, 1–11, *Online ahead of print*.
21. Ahmad, S.; Bano, N.; Qazi, S.; Yadav, M.K.; Ahmad, N.; Raza, K. Multitargeted molecular dynamic understanding of butoxypheser against SARS-CoV-2: An in silico study. *Nat. Prod. Commun.* **2022**, *17*, 1934578X221115499.
22. Ahmad, S.; Bhanu, P.; Kumar, J.; Pathak, R.K.; Mallick, D.; Uttarkar, A.; Mishra, V. Molecular dynamics simulation and docking analysis of NF-κB protein binding with sulindac acid. *Bioinformation* **2022**, *18*, 170–179.
23. Ahmad, S.; Dahiya, V.; Vibhuti, A.; Pati Pandey, P.; Tripathi, M.K.; Yadav, M.K. Protein-Based Therapeutics. In *Therapeutic Protein-Based Vaccines*; Springer: Berlin/Heidelberg, Germany, 2023; pp. 355–384.
24. Ahmad, S.; Pasha Km, M.; Raza, K.; Rafeeq, M.M.; Habib, A.H.; Eswaran, M.; Yadav, M.K. Reporting dinaciclib and theodrenaline as a multitargeted inhibitor against SARS-CoV-2: An in-silico study. *J. Biomol. Struct. Dyn.* **2023**, *41*, 4013–4023.

25. Ahmad, S.; Chitkara, P.; Khan, F.N.; Kishan, A.; Alok, V.; Ramlal, A.; Mehta, S. Mobile technology solution for COVID-19: Surveillance and prevention. In *Computational Intelligence Methods in COVID-19: Surveillance, Prevention, Prediction and Diagnosis*; Springer: Berlin/Heidelberg, Germany, 2021; pp. 79–108.
26. Ahmad, S.; Raza, K. Identification of 5-nitroindazole as a multitargeted inhibitor for CDK and transferase kinase in lung cancer: A multisampling algorithm-based structural study. *Mol. Divers.* **2023**, 1–14.
27. Ahmad, S.; Sheikh, K.; Bano, N.; Rafeeq, M.M.; Mohammed, M.R.S.; Yadav, M.K.; Raza, K. Nature-Inspired Intelligent Computing Techniques in Bioinformatics. In *Illustrious Implications of Nature-Inspired Computing Methods in Therapeutics and Computer-Aided Drug Design*; Springer Nature: Singapore, 2022; pp. 293–308.
28. Ahmad, S.; Singh, V.; Gautam, H.K.; Raza, K. Multisampling-based docking reveals Imidazolidinyl urea as a multitargeted inhibitor for lung cancer: An optimisation followed multi-simulation and in-vitro study. *J. Biomol. Struct. Dyn.* **2023**, 1–18.
29. Rose, P.W.; Beran, B.; Bi, C.; Bluhm, W.F.; Dimitropoulos, D.; Goodsell, D.S.; Prlić, A.; Quesada, M.; Quinn, G.B.; Westbrook, J.D.; et al. The RCSB Protein Data Bank: Redesigned web site and web services. *Nucleic Acids Res.* **2010**, *39*, D392–D401.
30. Schrödinger, L. *Maestro*; Schrödinger Release 2; Schrödinger, LLC: New York, NY, USA, 2020.
31. Release, S. *Protein Preparation Wizard*; Epik, Schrödinger, LLC: New York, NY, USA, 2016.
32. Tripathi, M.K.; Ahmad, S.; Tyagi, R.; Dahiya, V.; Yadav, M.K. Computer Aided Drug Design (CADD): From Ligand-Based Methods to Structure-Based Approaches. In *Chapter 5—Fundamentals of Molecular Modeling in Drug Design*; Elsevier: Amsterdam, The Netherlands, 2022; pp. 125–155.
33. Yadav, M.K.; Ahmad, S.; Raza, K.; Kumar, S.; Eswaran, M.; Pasha Km, M. Predictive modeling and therapeutic repurposing of natural compounds against the receptor-binding domain of SARS-CoV-2. *J. Biomol. Struct. Dyn.* **2022**, *41*, 1527–1539.
34. Release, S. *Prime*; Schrödinger, LLC: New York, NY, USA, 2020.
35. Jacobson, M.P.; Pincus, D.L.; Rapp, C.S.; Day, T.J.F.; Honig, B.; Shaw, D.E.; Friesner, R.A. A hierarchical approach to all-atom protein loop prediction. *Proteins Struct. Funct. Bioinform.* **2004**, *55*, 351–367.
36. Release, S. *Epik*; Schrödinger Release 1; Schrödinger, LLC: New York, NY, USA, 2020.
37. Li, H.; Robertson, A.D.; Jensen, J.H. Very fast empirical prediction and rationalization of protein pKa values. *Proteins Struct. Funct. Bioinform.* **2005**, *61*, 704–721.
38. Jorgensen, W.L.; Maxwell, D.S.; Tirado-Rives, J. Development and testing of the OPLS all-atom force field on conformational energetics and properties of organic liquids. *J. Am. Chem. Soc.* **1996**, *118*, 11225–11236.
39. Jorgensen, W.L.; Tirado-Rives, J. The OPLS [optimized potentials for liquid simulations] potential functions for proteins, energy minimizations for crystals of cyclic peptides and crambin. *J. Am. Chem. Soc.* **1988**, *110*, 1657–1666.
40. Huang, R.; Southall, N.; Wang, Y.; Yasgar, A.; Shinn, P.; Jadhav, A.; Nguyen, D.-T.; Austin, C.P. The NCGC pharmaceutical collection: A comprehensive resource of clinically approved drugs enabling repurposing and chemical genomics. *Sci. Transl. Med.* **2011**, *3*, 80ps16.
41. Release, S. *LigPrep*; Schrödinger, LLC: New York, NY, USA, 2019.
42. Friesner, R.A.; Murphy, R.B.; Repasky, M.P.; Frye, L.L.; Greenwood, J.R.; Halgren, T.A.; Sanschagrin, P.C.; Mainz, D.T. Extra precision glide: Docking and scoring incorporating a model of hydrophobic enclosure for protein− ligand complexes. *J. Med. Chem.* **2006**, *49*, 6177–6196.
43. Release, S. *Glide*; Schrödinger Release 3; Schrödinger, LLC: New York, NY, USA, 2021.
44. Lipinski, C.A. Lead-and drug-like compounds: The rule-of-five revolution. *Drug Discov. Today Technol.* **2004**, *1*, 337–341.
45. Release, S. *QikProp*; Schrödinger, LLC: New York, NY, USA, 2020.
46. Alghamdi, Y.S.; Mashraqi, M.M.; Alzamami, A.; Alturki, N.A.; Ahmad, S.; Alharthi, A.A.; Alshamrani, S.; Asiri, S.A. Unveiling the multitargeted potential of N-(4-Aminobutanoyl)-S-(4-methoxybenzyl)-L-cysteinylglycine (NSL-CG) against SARS CoV-2: A virtual screening and molecular dynamics simulation study. *J. Biomol. Struct. Dyn.* **2023**, *41*, 6633–6642.
47. Alturki, N.A.; Mashraqi, M.M.; Alzamami, A.; Alghamdi, Y.S.; Alharthi, A.A.; Asiri, S.A.; Alshamrani, S. In-silico screening and molecular dynamics simulation of drug bank experimental compounds against SARS-CoV-2. *Molecules* **2022**, *27*, 4391.

48. Alzamami, A.; Alturki, N.A.; Alghamdi, Y.S.; Ahmad, S.; Alshamrani, S.; Asiri, S.A.; Mashraqi, M.M. Hemi-Babim and fenoterol as potential inhibitors of MPro and papain-like protease against SARS-CoV-2: An in-silico study. *Medicina* **2022**, *58*, 515.
49. Bhati, R.; Nigam, A.; Ahmad, S.; Raza, K.; Singh, R. Structural–functional analysis and molecular characterization of arsenate reductase from Enterobacter cloacae RSC3 for arsenic biotransformation. *3 Biotech* **2023**, *13*, 305.
50. Famuyiwa, S.O.; Ahmad, S.; Fakola, E.G.; Olusola, A.J.; Adesida, S.A.; Obagunle, F.O.; Raza, K.; Ugwo, J.P.; Oyelekan, E.I.; Faloye, K.O. Comprehensive computational studies of naturally occurring kuguacins as antidiabetic agents by targeting visfatin. *Chem. Afr.* **2023**, *6*, 1415–1427.
51. Hou, J.; Bhat, A.M.; Ahmad, S.; Raza, K.; Qazi, S. In silico analysis of ACE2 receptor to find potential herbal drugs in COVID-19 associated neurological dysfunctions. *Nat. Prod. Commun.* **2022**, *17*, 1934578X221118549.
52. Bochevarov, A.D.; Harder, E.; Hughes, T.F.; Greenwood, J.R.; Braden, D.A.; Philipp, D.M.; Rinaldo, D.; Halls, M.D.; Zhang, J.; Friesner, R.A. Jaguar: A high-performance quantum chemistry software program with strengths in life and materials sciences. *Int. J. Quantum Chem.* **2013**, *113*, 2110–2142.
53. Schrödinger, L. *Jaguar*; Schrödinger release 4; Schrödinger, LLC: New York, NY, USA, 2015.
54. Bowers, K.J.; Chow, E.; Xu, H.; Dror, R.O.; Eastwood, M.P.; Gregersen, B.A.; Klepeis, J.L.; Kolossvary, I.; Moraes, M.A.; Sacerdoti, F.D.; et al. Scalable Algorithms for Molecular Dynamics Simulations on Commodity Clusters. In Proceedings of the 2006 ACM/IEEE Conference on Supercomputing, November 2006; p. 84-es. Available online: **https://dl.acm.org/doi/abs/10.1145/1188455.1188544** (accessed on 1 February 2024).
55. Release, S. *Desmond Molecular Dynamics System*; DE Shaw Research: New York, NY, USA, 2017.
56. Mark, P.; Nilsson, L. Structure and dynamics of the TIP3P, SPC, and SPC/E water models at 298 K. *J. Phys. Chem. A* **2001**, *105*, 9954–9960.
57. McDonald, I. NpT-ensemble Monte Carlo calculations for binary liquid mixtures. *Mol. Phys.* **1972**, *23*, 41–58.
58. Rawluk, J.; Waller, C.F. Gefitinib. *Small Mol. Oncol.* **2018**, *211*, 235–246.
59. Herbst, R.S.; Fukuoka, M.; Baselga, J. Gefitinib—A novel targeted approach to treating cancer. *Nat. Rev. Cancer* **2004**, *4*, 956–965.
60. Maemondo, M.; Inoue, A.; Kobayashi, K.; Sugawara, S.; Oizumi, S.; Isobe, H.; Gemma, A.; Harada, M.; Yoshizawa, H.; Kinoshita, I.; et al. Gefitinib or chemotherapy for non–small-cell lung cancer with mutated EGFR. *N. Engl. J. Med.* **2010**, *362*, 2380–2388.